The Journal of Chemical Physics

Dynamical anomalies and structural features of active Brownian particles characterized by two repulsive length scales

Cite as: J. Chem. Phys. **156**, 164502 (2022); https://doi.org/10.1063/5.0087601
Submitted: 07 February 2022 • Accepted: 07 April 2022 • Accepted Manuscript Online: 08 April 2022 • Published Online: 26 April 2022

José Martín-Roca, Raúl Martinez, Fernando Martínez-Pedrero, et al.

The Journal of Chemical Physics ARTICLE scitation.org/journal/jcp

Dynamical anomalies and structural features of active Brownian particles characterized by two repulsive length scales

Cite as: J. Chem. Phys. 156, 164502 (2022); doi: 10.1063/5.0087601
Submitted: 7 February 2022 • Accepted: 7 April 2022 •
Published Online: 26 April 2022

José Martín-Roca,[1] Raúl Martinez,[1,2] Fernando Martínez-Pedrero,[3] Jorge Ramírez,[4] and Chantal Valeriani[1,5,a)]

AFFILIATIONS

[1] Dep. de Est. de la Materia, Física Térmica y Electrónica, Universidad Complutense de Madrid, 28040 Madrid, Spain
[2] Dep. de Física Teórica de la Materia Condensada, Facultad de Ciencias, Universidad Autónoma de Madrid, 28049 Madrid, Spain
[3] Dep. Química-Fisica, Universidad Complutense de Madrid, Avda. Complutense s/n, Madrid 28040, Spain
[4] Dep. de Ingeniería Química, ETSI Industriales, Universidad Politécnica de Madrid, 28006 Madrid, Spain
[5] GISC - Grupo Interdisciplinar de Sistemas Complejos, 28040 Madrid, Spain

Note: This paper is part of the JCP Special Topic on Slow Dynamics.
[a)] **Author to whom correspondence should be addressed:** cvaleriani@ucm.es

ABSTRACT

In this work, we study a two-dimensional system composed by Active Brownian Particles (ABPs) interacting via a repulsive potential with two length scales—a soft shell and a hard core. Depending on the ratio between the strength of the soft shell barrier and the activity, we find two regimes: If this ratio is much larger or smaller than 1, the observed behavior is comparable with ABPs interacting via a single length scale potential. If this ratio is similar to 1, the two length scales are relevant for both structure and dynamical properties. On the structural side, when the system exhibits a motility induced phase separation, the dense phase is characterized by new and more complex structures compared with the hexatic phase observed in single length scale systems. From the dynamic analysis, we find, to our knowledge, the first manifestation of a dynamic heterogeneity in active particles, reminiscent of the glassy dynamics widely studied in passive colloids.

I. INTRODUCTION

Active particle suspensions are out-of-equilibrium systems in which particles dissipate energy and transform it into motion.[1,2] A characteristic feature of active particles is collective motion, observed both in active living systems[3] (such as bacteria colonies or a flock of birds) as well as in synthetic active particles.[4,5] One of the simplest numerical models introduced to better understand the physics of active particles is the so-called Active Brownian Particles (ABPs). ABPs follow the equations of motion of Brownian dynamics, modified to allow self-propulsion and gradual change of the direction of particle motion by rotational diffusion. When ABPs interact repulsively at relatively high density and activity, particles tend to exhibit a process called Motility Induced Phase Separation (MIPS), despite the absence of explicit attractive forces. MIPS[6–12] is promoted by the greater persistence length supported by the activity, as compared to that sustained by the thermal rotational diffusion. It has recently been shown[13–17] that the steepness of the repulsion plays a role in the establishment of MIPS phase boundaries.

Even though the MIPS dense phase is an assembly of geometrically frustrated particles, it does not display any glassy feature, such as a dynamical slowing down.[18]

A glass transition has been encountered in driven granular media, active and living matter.[19] Even though important features of glassy dynamics are insensitive to details, the location of the transition depends on the specifics of the driving mechanisms. When increasing the packing fraction, even a suspension of self-propelled repulsive spheres undergoes a dynamic slowing down. However, differently from a passive system, the glass transition can be shifted to higher packing fractions upon increasing the activity.[20]

An active glass is fundamentally different from an equilibrium glassy system. Activity does not simply fluidize the system[21]

but increases the dynamic heterogeneities, even for the same relaxation times. Glass theories, such as the random first-order transition (RFOT) theory, have been extended to a dense assembly of self-propelled particles,[22] showing that the behavior of the active glass is strongly influenced by the microscopic details of activity. The authors of Ref. 23 studied the dynamics of a dense binary Lennard-Jones mixture of active particles (considering inertia). They demonstrated that tuning the persistence time, the system underwent a crossover between a glassy behavior (characterized by density relaxation) and a jamming behavior. Only very recently, the glass transition has been studied in a suspension of complex active particles: a dense solution of circular active polymers.[24] In this system, the interplay between activity and topology of the polymers generated a unique glassy state.

To the best of our knowledge, investigations on active Brownian particles to date have focused on repulsive interactions with one characteristic length scale, i.e., excluded-volume interactions. When dealing with equilibrium (passive) systems, it has been shown that it is possible to generate water-like behavior (including its anomalies) when particles interact through isotropic potentials with two characteristic length scales: a hard core (short-range) repulsion combined with soft-shell (long-range) repulsion.[21,25–38] This shoulder-type interaction potential has been also used to simulate equilibrium suspensions of block copolymers or colloidal spheres decorated with filaments on their surface.[39] These systems are characterized by a very rich phase behavior, with various ordered structures, in two[40–42] or three dimensions, which is in contrast with the phase behavior observed in a suspension of particles interacting via a single repulsive core. Malescio and Pellicane[40] demonstrated that, in a two-dimensional suspension of colloids interacting via a shoulder-type potential, at densities where hard-and-soft core radii compete with each other, the decrease in temperature induces a transition from a disordered state to an orientationally ordered phase characterized by stripe patterns. In three-dimensional suspensions, a surprisingly complex phase behavior has also been established.[41] The authors detected density and diffusion anomalies similar to those in water and concluded that the anomalies disappeared as the width of the repulsive step increased, shifting to the regions inside the crystalline phase in the vicinity of the maximum of the melting line.

These anomalous features appeared not only in complex liquids[41,43,44] but also in silica[45] and in colloidal systems.[46] Considering passive colloidal particles interacting via two repulsive length scales, the authors of Ref. 47 demonstrated that such systems presented a logarithmic decay of the density autocorrelation function and a subdiffusive regime in the mean-square displacement.[48] Such anomalous dynamics had also been detected in the reentrant glass behavior that emerges in a system of passive hard spheres with short-range attraction,[49] caused by the existence of two different glassy states: one dominated by repulsion (with structural arrest due to caging) and the other dominated by attraction (with structural arrest due to bonding). Thus, the anomalous dynamics was a sign of competing glass transitions in core-softened systems and in repulsive systems with two competing length scales.

In this work, we study a two-dimensional suspension of ABPs interacting with a repulsive shoulder-type potential to unravel how two length scales affect both the structural behavior and the dynamics of the suspension.

II. SIMULATION DETAILS

A. Numerical details

The system consists of N Active Brownian Particles (ABPs) interacting through a hard core potential surrounded by a soft corona.[40] Particles are located in a two-dimensional box of area $A = L \times L$ with periodic boundary conditions. The equations of motion for the position $\vec{r}_i$ and orientation θ_i of the ith active particle can be written as

$$\dot{\vec{r}}_i = \frac{D_t}{k_B T}\left(-\sum_{j\neq i}\nabla V(r_{ij}) + |F_a|\,\vec{n}_i\right) + \sqrt{2D_t}\,\vec{\xi}_i, \tag{1}$$

$$\dot{\theta}_i = \sqrt{2D_r}\,\xi_{i,\theta}, \tag{2}$$

where $V(r_{ij})$ is the inter-particle pair potential, k_B is the Boltzmann constant, T is the absolute temperature, the components of $\vec{\xi}_i$ and $\xi_{i,\theta}$ are white noise with zero mean and correlations $\langle \xi_i^\alpha(t)\xi_j^\beta(t')\rangle = \delta_{ij}\delta_{\alpha\beta}\delta(t-t')$, being $\alpha,\beta = x,y$, F_a is a constant self-propelling force acting along the vector $\vec{n}_i$, which forms an angle θ_i with the positive x axis, and D_t and D_r are the translational and rotational diffusion coefficients, respectively. For spherical particles at equilibrium, the relation between both coefficients obeys the Stokes–Einstein relation:[50] $D_r = 3D_t/\sigma^2$, where σ is the hard core diameter. The inter-particle potential is characterized by two different length scales: a repulsive hard core and a soft repulsive shoulder, given as follows:[41]

$$V(r) = \varepsilon\left(\frac{\sigma}{r}\right)^n + \frac{1}{2}\,\varepsilon_s\,\{1-\tanh[k_0\,(r-\sigma_s)]\}, \tag{3}$$

where ε is the energy related to the hard core, ε_s and σ_s are the height and width of the repulsive shoulder, respectively, n affects the stiffness of the repulsive core, and k_0 determines the steepness of the shoulder decay [Fig. 1(a)]. Throughout this work, we have chosen to establish the following parameters: $n = 14$ and $k_0 = 10/\sigma$ as in Ref. 41, and $\sigma_s = 2.5\sigma$. In order to study the time evolution of the system, we have used the open source code Large-scale Atomic/Molecular Massively Parallel Simulator (LAMMPS);[51] when dealing with the $N = 2^{14}$ systems, however, we have used a modified version of UAMMD[52] (Universally Adaptable Multiscale Molecular Dynamics). Each simulation has been reiterated until the system attains steady state, which we assume arrives when there are no further significant changes in potential energy and overall phase behavior. The level of activity is measured via the Peclet number, defined as

$$\mathrm{Pe} \equiv \frac{3\,v_p\,\tau_r}{\sigma} = \frac{3\,|F_a|\,D_t}{k_B\,T\,D_r\,\sigma}, \tag{4}$$

where $v_p = |F_a|D_t/k_BT$ is the velocity propulsion of the active particles and $\tau_r = 1/D_r$ is the reorientation time. Throughout this manuscript, we have varied the Peclet number by changing D_r, keeping all other parameters fixed. Other ways to modify Pe (for example, by changing magnitude of the active force) yield slightly different phase behavior.[17] All quantities are expressed in reduced Lennard-Jones units, with lengths, times, and energies given in terms of $\sigma = \tau = \varepsilon = 1$, where $\tau = \sqrt{m\sigma^2/\varepsilon}$. The time step has been set to $\Delta t/\tau = 5 \cdot 10^{-5}$, with $D_t\tau/\sigma^2 = k_BT$. The reduced temperature is set

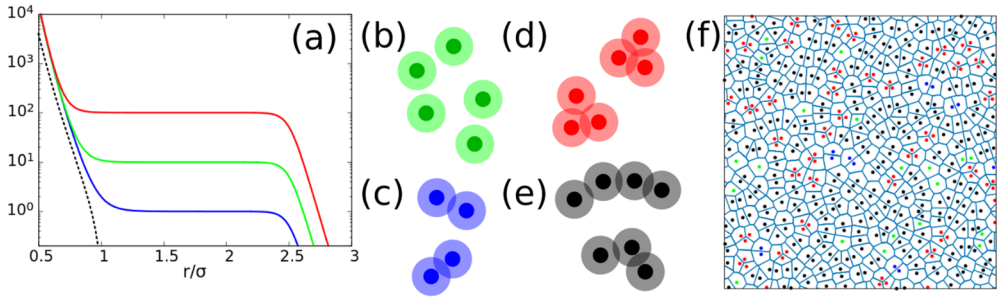

FIG. 1. (a) Semilogarithmic representation of the repulsive potential $V(r)$ vs r/σ [see Eq. (3)] for different values of the shoulder height: $\varepsilon_s = 1$ (blue), $\varepsilon_s = 10$ (green), and $\varepsilon_s = 100$ (red). The remaining parameters adopt the values indicated in the text. The Weeks–Chandler–Andersen (WCA) potential is shown (black dashed line) for comparison purposes. (b)–(e) Examples of different local structures observed in our simulations: monomers [(b), green], dimers [(c), blue], trimers [(d), red], and chains [(e), black]. (f) Voronoi tessellation of a steady-state snapshot taken from a simulation with Pe = 25 and $\varepsilon_s = 10$. Each of the particles that make up the local structures is represented by the corresponding color, as described above.

to $k_BT/\varepsilon = 0.1$ to reduce the role played by the thermal noise. Note that, in our simulations, the rotational and translational diffusivities D_r and D_t are not coupled by the Einstein–Stokes relation $D_r = 3D_t/\sigma^2$ because this relation is strictly true only at equilibrium. In this work, we consider three different shoulder heights of $\varepsilon_s/\varepsilon = 1, 10$, and 100, and the velocity propulsion of each active particle is $v_p\tau/\sigma = 10$. In addition, the number density $\rho = N/L^2$ ranges from 0.01 up to about 1.

B. Analysis tools: Detection of MIPS

By implementing Fortune's algorithm, we compute the Voronoi tessellation, the area available to each particle, and the local density, which has been traditionally used to detect the onset of MIPS. When this function presents just one mode, the particles form a one-phase system, whereas when the distribution is clearly bimodal, they are segregated to form an MIPS system, characterized by areas of high and low density. Recently, other tools have been used to identify MIPS in ABPs systems. For example, it has been shown that ABPs interacting via WCA[53] potential show non-Gaussian displacements at intermediate times. This can be detected by means of the following two-dimensional non-Gaussian parameter.[17] This parameter measure the deviation between the displacement distribution function with respect to the Gaussian distribution, characteristic of pure Brownian motion. The non-Gaussian parameter is traditionally used to describe anomalous and/or heterogeneous transport dynamics in equilibrium systems or approaching the glassy state.

C. Analysis tools: Identifying complex structures

Although the shoulder-type potential shown in Eq. (3) has spherical symmetry, it has been shown to produce a rich variety of phases.[40] When the particles are active, the system reaches states with density distributions showing more than two peaks. To identify each of the phases appearing in the system and to help detect MIPS, we have developed the next structure classification algorithm. As shown in Figs. 1(b)–1(f), particles interacting via a shoulder-like potential present different types of local structures. The different local structures are characterized, in part, by being made up of a number of particles that have at least one neighbor closer than a certain fixed limit that connect the particles, $r_c = 1.7\sigma$. This cutoff value, in the range between the hard core and shoulder radii, has been carefully chosen so that particles whose shoulders overlap are considered as belonging to the same structure, while particles belonging to the second layer are not. After imposing the above criteria, we apply the following classification:

- *Monomers* are structures composed by only one particle [see Fig. 1(b)].
- *Gas-like* phase is composed by a set of monomers with a local density, ρ_0, smaller than $\rho_c = 0.145\sigma^2$, which corresponds to the close packing of particles with diameter $\sigma_s/\sigma = 2.5$.
- *Dimers* are structures composed by two connected particles [see Fig. 1(c)].
- *Trimers* are structures composed of three particles, all with the other two particles at a distance of less than $r_c = 1.7\sigma$ [see Fig. 1(d)].
- *Chains* are structures formed by N particles $(N > 2)$ in which all particles are connected with less than four neighbors not connecting each other. Hence, chains can be very long and may have branches [Fig. 1(e)].
- Other complex structures are simply classified as *dense phase*, and in them the constituent particles connected with more than three neighbors, or there are three neighbors connecting each other.

In these structures, hexagonal order is detected by computing the hexagonal order parameter for each particle,

$$\psi_6(k) = \frac{1}{n}\sum_{j\in N_k} e^{i\,6\,\theta_{kj}}, \tag{5}$$

where θ_{kj} is the angle between the vector $\vec{r}_{kj}$ and the x axis and N_k is the set of first Voronoi neighbors[54] of particle k. Note that the hexagonal order appears both in the diluted and dense phases.

D. Analysis tools: Computing the pressure within the system

How to compute pressure in non-equilibrium systems is still under debate. In active particle suspensions, some works[55–59] have proposed expressions analogous to state equations that include terms accounting for activity. In 2D ABP systems, the total pressure can be computed as[60]

$$P = \frac{Nk_BT}{A} + \frac{\gamma v_p}{2AD_r}\sum_{i=1}^{N}\langle \vec{n}_i \cdot \dot{\vec{r}}_i \rangle + \frac{1}{4A}\sum_{i=1}^{N}\sum_{j=1}^{N}\vec{F}_{ij}\cdot\vec{r}_{ij}, \quad (6)$$

where $\gamma = K_BT/D_t$ is the friction coefficient and the sum over the particles includes the contribution from the periodic boundary conditions.[61] $\dot{\vec{r}}_i$ can be computed by using Eq. (1), discarding the thermal noise, which has a small value compared to the other two terms. Note that the first term represents the ideal gas pressure, the second is the activity contribution, the so-called swimming pressure, P_s, and the last term includes the contribution of the interaction potential. Hence, we can compute the local contribution of each particle ith to the pressure as

$$P_i^{(L)} = \frac{\gamma v_p}{2AD_r}\vec{n}_i \cdot \dot{\vec{r}}_i + \frac{1}{4A}\sum_{j=1}^{N}\vec{F}_{ij}\cdot\vec{r}_{ij}, \quad (7)$$

the first term due to the activity and the second one including the contribution of the interaction potential.

E. Analysis tools: Dynamical properties

The relaxation dynamics of glasses is frequently examined by studying the decay of the self (incoherent) intermediate scattering function,

$$F(\vec{q},t) = \frac{1}{N}\sum_{j=1}^{N}\langle \exp[i\vec{q}\cdot(\vec{r}_j(t) - \vec{r}_j(0))]\rangle, \quad (8)$$

where $\vec{r}_j(0)$ is the position of particle j once the steady-state is reached (and time is set to 0) and $\vec{q}$ is the wave vector. Assuming that the stationary regime is isotropic and, thus, the intermediate scattering function only depends on the modulus of q and time, we analyze the decay of $F(q^*,t)$, where q^* is the smallest value of q at which the static structural factor $S(q)$ shows a maximum. For a better understanding of the dynamics, we also compute the Mean Square Displacement (MSD),

$$MSD(t) = \langle |\boldsymbol{r}(t) - \boldsymbol{r}(0)|^2 \rangle, \quad (9)$$

as well as the long time effective diffusion coefficient D_{eff}, defined as the slope of the MSD at long times.

Inspired by Refs. 62–64, we have estimated the velocity fields when the system undergoes MIPS (see the supplementary material for more details). The velocity field has been computed as the displacement of the particles between two times $\vec{v} = \frac{\vec{x}(t+\tau)-\vec{x}(t)}{\tau}$, where τ is the unit of time.

III. RESULTS

In this work, we first study different structural properties of ABPs suspensions characterized by various values of the shoulder height. Next, we unravel their dynamical features.

A. Structural features

1. Soft ($\varepsilon_s/\varepsilon = 1$) and hard ($\varepsilon_s/\varepsilon = 100$) shoulder heights

To begin with, we explore the phase diagram of active particles interacting with a soft shoulder potential with height, $\varepsilon_s/\varepsilon = 1$. Under these conditions, active particles can easily overcome the shoulder of the potential generated by their neighbors and behave as if they have an effective diameter $\sigma_{eff} \approx \sigma$. Figure 2 shows the ρ-Pe phase behavior of such suspension (red squares). As in the case of WCA, for low ρ and Pe, the system is in a homogeneous state (empty squares), whereas when both the density and Peclet number simultaneously increase, the system exhibits MIPS (filled squares). As expected, when the repulsive barrier height is low and can be easily overcome by the active particles, the phase diagram is not affected by the presence of a second length scale, being essentially the same as that of particles interacting through a WCA potential. Next, we explore the system when $\varepsilon_s/\varepsilon = 100$. In this limit, particles behave as if they have an effective diameter $\sigma_{eff} \approx \sigma_s$. Therefore, the phase diagram is similar to that exhibited when particles with diameter σ_s interact via a WCA potential. In Fig. 2, different states depicted by the ABPs interacting through a shoulder potential with $\varepsilon_s/\varepsilon = 100$ are shown with the filled or empty blue symbols. It is evident that both phase diagrams approximately coincide when the density and Pe number are properly scaled, except for two clear differences: (i) The boundaries differ slightly at the lower limits of ρ and Pe due to differences existing between the slopes of the soft shell and the hard core potentials [see Fig. 1(a)] and (ii) at high density, the particles are allowed to overlap because even though the shoulder of the soft shell potential is rather high, the repulsion does not diverge to infinity.

In order to unravel whether the shape of the interaction potential plays a role in the structures formed, we analyze a global structural property, such as the radial distribution function. Figures 3(a) and 3(b) show the radial distribution functions and the

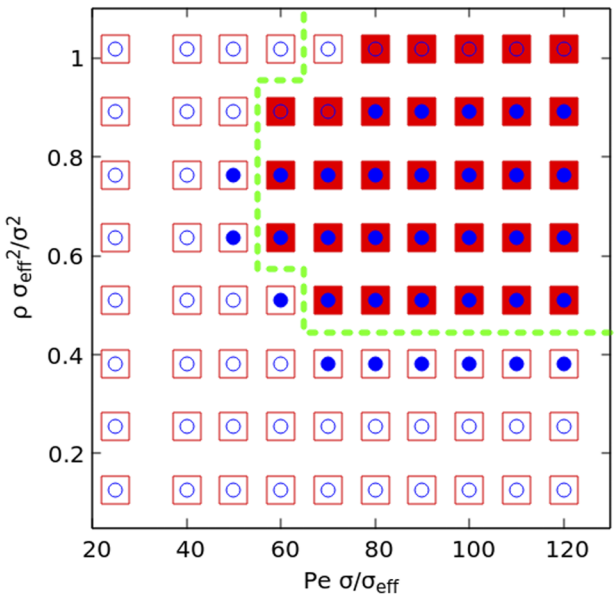

FIG. 2. Phase behavior for a suspension of ABPs interacting through the shoulder-like potential with $\varepsilon_s/\varepsilon = 1$ (red squares) and $\varepsilon_s/\varepsilon = 100$ (blue dots). Peclet is modified by changing D_r, while keeping fixed $v_p = 10$, $k_BT = 0.1$, and $D_t = 0.1$. The density and Pe axes were scaled ($\rho_{eff} = \sigma_s^2 \cdot \rho$ and $\mathrm{Pe}_{eff} = \frac{Pe}{\sigma_s}$) so that both phase diagrams (for $\varepsilon_s/\varepsilon = 1$ and 100) can be shown on the same plot. The empty symbols represent the system in a homogeneous phase and filled symbols in an MIPS phase. The green dashed line shows the onset of the MIPS regime when particles interact via a WCA potential.

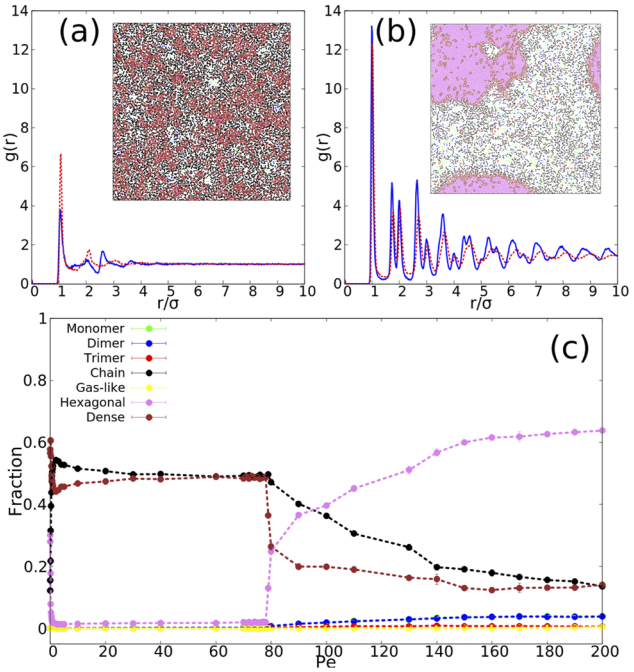

FIG. 3. (a) and (b) Radial distribution functions for a system in the homogeneous [Pe = 50, (a)] and MIPS states [Pe = 120, (b)], when particles interact through the two lengths scale repulsive potential with $\varepsilon_s/\varepsilon = 1$ (blue continuous line and corresponding snapshots) or the WCA potential (red dashed line). (c) Average percentage of monomers (green), dimers (blue), trimers (red), chains (black), high hexagonal order (violet), gas-like (yellow), and dense structures (brown) as a function of the Peclet for particles interacting via a shoulder-like potential with $\varepsilon_s/\varepsilon = 1$. In all calculations, $\rho\sigma^2 = 0.509$.

corresponding snapshots for a system characterized by $\varepsilon_s/\varepsilon = 1$ (in blue), at low and high Peclet number [Pe = 50 and 120, (a) and (b), respectively]. The results are compared to those obtained when ABPs interact through a WCA potential (red dashed line). In the homogeneous states, the radial distribution functions present two peaks when the ABPs interact via the shoulder potential, the first at the hard core distance and the second at the soft-shell distance, and only one when ABPs interact through the WCA potential. In the MIPS state [high Pe, Fig. 3(b)], the $g(r)$ presents many peaks, which is a characteristic of a highly ordered or crystalline structure. When comparing to the system where ABPs interact via a WCA potential [red dashed lines in Figs. 3(a) and 3(b)], we observe that the latter exhibits a similarly ordered structure. This supports the idea that the MIPS states in both systems are very similar. The visual inspection of the snapshots shows that, in the homogeneous state, most particles in the system are chain and dense structures. In the MIPS state, mostly dimers, chains, or trimers are found in the low density regions. The high density phases are comprised by different species. The interior of the high density phases consists of hexagonal lattice domains separated by boundaries. In the regions between the high and low density phases, particles arrange in chain-like structures.

In order to study how the structure distribution changes as a function of activity, we focus on a system composed of ABPs interacting via the shoulder-like potential, at a given density ($\rho\sigma^2 = 0.509$) and quantify how the populations of different particle types change as a function of activity. Figure 3(c) shows the average fraction of different types of structures computed at different Peclet numbers. At a low Peclet number, when the system is in a homogeneous state, it mostly consists of dense and chain-like structures [as shown in the corresponding snapshot in Fig. 3(a)]. At a high Peclet number, we detect an increase in the percentage of structure with hexagonal order. When the system enters in the MIPS state (around Pe ≈ 75 at $\rho\sigma^2 = 0.509$), most of the chains become ordered and transform into hexagonal phase, whereas the other phases change only slightly. For the sake of comparison, we have checked that, under the same conditions, when ABPs interact through a WCA potential, particles only arrange in a dense hexagonal state for larger values of the Peclet number.

2. When repulsion strength competes with activity

When $\varepsilon_s/\varepsilon = 10$, the propulsion magnitude v_p is not large enough for the particles to easily overcome the repulsive barrier of the corona as in the case when $\varepsilon_s/\varepsilon = 1$. On the other hand, the shoulder barrier is not high enough to prevent particle overlapping, as in the case when $\varepsilon_s/\varepsilon = 100$. Here, the soft repulsive shell starts playing an important role in the phase behavior of the system. Figure 4 shows the ρ-Pe state diagram of such suspensions. Here, both length scales are important and, therefore, it is not possible to scale the axes like in Fig. 2 for the cases $\varepsilon_s/\varepsilon = 1$ and $\varepsilon_s/\varepsilon = 100$. As compared to the case when $\varepsilon_s/\varepsilon = 1$ (Fig. 2), here the MIPS region shifts to lower densities and higher values of the Peclet number (compare axis ranges in Figs. 2 and 4). In the cases when $\varepsilon_s/\varepsilon = 1$ and 100, MIPS is typically detected when the high density phase appears and the density distribution becomes bimodal. However, when $\varepsilon_s/\varepsilon = 10$, the density distribution does not become clearly bimodal without showing

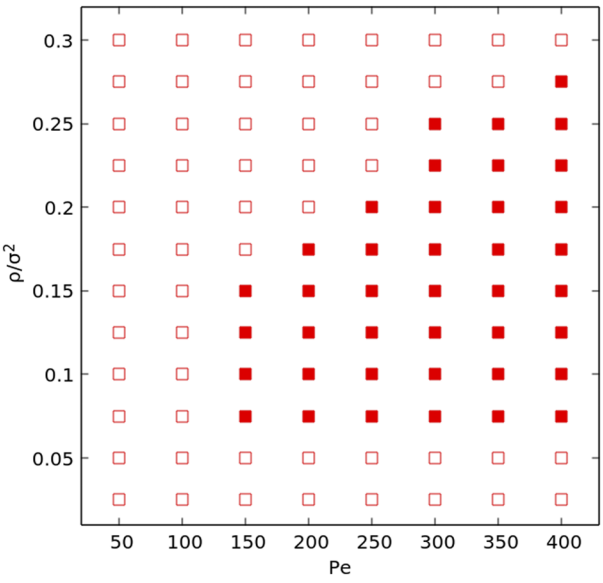

FIG. 4. Phase behavior for a suspension of ABPs interacting through a shoulder-like potential with $\varepsilon/\varepsilon_s = 10$. Peclet is varied changing D_r, while keeping fixed $v_p = 10$, $k_BT/\varepsilon = 0.1$, and $D_t\tau^2/\sigma = 0.1$. Empty symbols represent the system in a homogeneous state and filled symbols in an MIPS state.

clear signs of MIPS, so even at Pe = 0 (so-called passive case), particles organize in areas with different characteristic densities. Only at very high Pe, a very low density phase is created and MIPS can be clearly detected. Therefore, the mechanism of MIPS formation is completely different from the cases where only one length scale is relevant and the MIPS state has perfect hexagonal order (see the supplementary material for more details about passive and active systems). In this case, detection of the MIPS boundary is slightly more complicated by means of the non-Gaussian parameter α_2 using the method described in Ref. 17. Figure 5 shows the radial distribution functions [panels (a) and (b)], the corresponding snapshots, and the fraction of particles classified into different structures [panel (c)] when $\varepsilon_s/\varepsilon = 10$ and $\rho\sigma^2 = 0.150$, slightly higher than the close-packing density $\rho_c/\sigma^2 \approx 0.145$. Figures 5(a) and 5(b) clearly show a homogeneous state at low Peclet number (Pe = 80) and an MIPS state at high Peclet number (Pe = 500).

In the homogeneous state [low Pe, in Fig. 5(a)], $g(r)$ presents several peaks, the highest one corresponding to the soft-shell distance (2.5σ). The peak at the hard core distance (σ) is due to the fraction of particles that form dimers [around 15% of the particles in the system, see Fig. 5(c)]. A visual inspection of a snapshot taken under the same conditions shows particles mostly colored in green (monomers) or blue (dimers). On the other hand, when the system is in an MIPS state [high Pe = 500, Fig. 5(b)], the peak at $r = \sigma$ increases significantly, which is a sign that many more particles have managed to jump over the shoulder of the potential. A visual inspection of a snapshot taken at the same state point [the inset in Fig. 5(b)] shows structures very different from the one presented in Fig. 3. While in the latter, the bulk of the dense phase mostly consisted of monomers surrounded by dimers; in the former, the bulk of the dense phase consists of chains and a few dimers and trimers surrounded by a layer of monomers, some of them arranged according to a crystalline order. In Fig. 3, we observe that the MIPS state shows a very well ordered hexagonal dense phase, with peaks in $g(r)$ that are periodically spaced, together with a high percentage of monomers arranged in hexagonal order. However, in Figs. 5(a) and 5(b), the peaks of $g(r)$ are more irregular, which is a sign of a more heterogeneous arrangement of particles inside the dense phase, with a significant percentage of particles forming chains, dimers, and trimers and a much smaller fraction of hexagonal monomer. At very high activity (Pe = 500), chains and dimers become the most frequent structure in the system, followed by trimers and monomers, with fewer hexagonal structures only present at the boundaries of the dense phase [Fig. 5(c)].

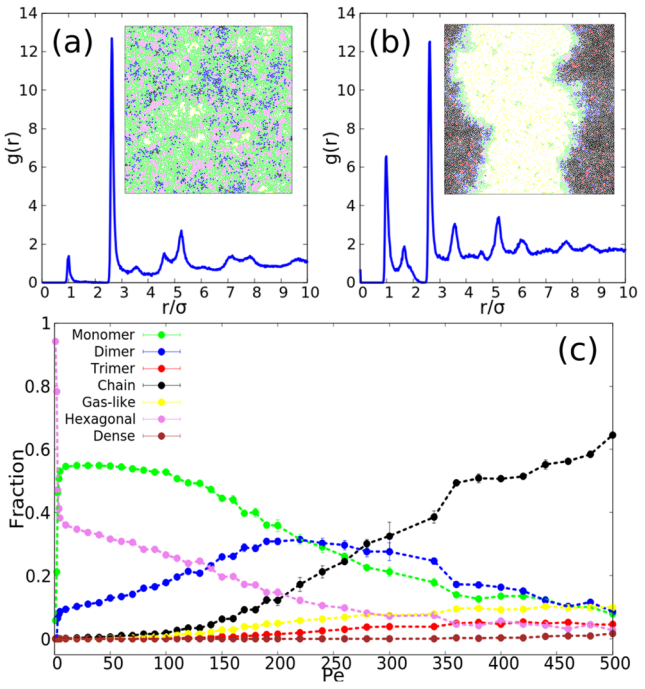

FIG. 5. (a) and (b) Radial distribution function and corresponding snapshots for a system at $\rho\sigma^2 = 0.150$ in the homogeneous state [Pe = 80, (a)] and MIPS state [Pe = 500, (b)]. (c) Average percentage of monomers (in green), dimers (in blue), chains (in black), trimers (in red), high hexagonal order (violet), gas phase (yellow), and dense phase (purple) as a function of the Peclet number for ABPs interacting though a shoulder-like potential with $\varepsilon_s/\varepsilon = 10$.

To conclude, we have explored the emergence of velocity correlations for three configurations that present MIPS with densities $\rho = 0.1, 0.2$, and 0.5. To better detect possible velocity correlations between particles within the dense phase, we have chosen to simulate these systems at very high activity (Pe = 5000). Figures are presented in the supplementary material. In all cases studied, a clear alignment of the velocity vectors has been detected inside the dense phase even when complex structures exist within. The same behavior has been observed in a system of ABP interacting only via a one length scale repulsive potential.[62–64]

3. Pressure

To better understand the structures formed within the separated phases reported in Figs. 3 and 5, we now compute both the global pressure and the local contribution to the pressure from each particle, Eqs. (6) and (7), respectively. Figure 6 shows the results obtained for two different cases, $\varepsilon_s/\varepsilon = 1$ (top) and $\varepsilon_s/\varepsilon = 10$ (bottom). Figures 6(a) and 6(b) show the snapshots of the system with $\varepsilon_s/\varepsilon = 1.0$, $\rho\sigma^2 = 0.509$, and Pe = 100, under conditions similar to those imposed in Fig. 3(b), colored according to the value of the swim pressure and the interaction pressure, respectively. In parallel, Figs. 3(d) and 3(e) show snapshots of the system with $\varepsilon_s/\varepsilon = 10.0$, $\rho\sigma^2 = 0.150$, and Pe = 500 [conditions as those imposed in Fig. 5(b)]. Both snapshots are taken in the MIPS region (see the corresponding phase diagrams in Figs. 2 and 4). Since the particles in the gas phase do not interact and their propulsion velocity is constant, the swimming pressure in the two exposed conditions [Figs. 6(a) and 6(d)] is similar for all particles in the gas phase. In the areas inside the dense regions, the interactive term in Eq. (7) is much larger than those due to the particle activity and to the thermal noise. Hence, from Eq. (1), we can compute the velocity of the particle $\dot{\vec{r}}_i \approx \frac{D_t}{k_B T}\vec{F}_i$, where $\vec{F}_i = \nabla V_i$ is the total conservative force acting over the particle. Here, we set $k_B T = 0.1$ and $D_t = 0.1$. However, in Eq. (7), the swimming pressure is given $P_s = \frac{\gamma v_p}{2 A D_r}\vec{n}_i \cdot \dot{\vec{r}}_i$. In the dense phase, the swimming pressure is given by $P_s = \frac{\gamma v_p k_B T}{2 A D_r D_t}\vec{n}_i \cdot \vec{F}_i$. Using this approximated equation, the negative pressure observed in the dense phase [Fig. 6(d)] is due to the events where $\vec{n}_i \cdot \vec{F}_i < 0$, i.e., when the interactions and active force acting on the particles

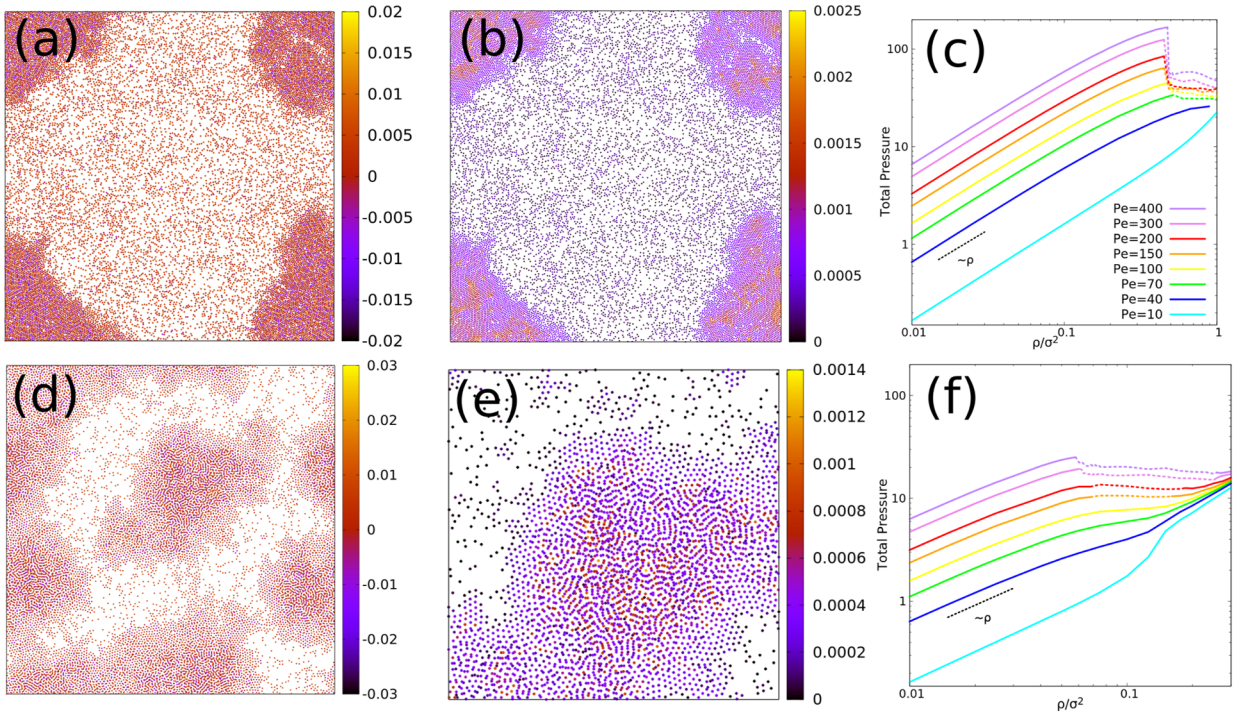

FIG. 6. Snapshots of the system for $\varepsilon_s/\varepsilon = 1$, $\rho\sigma^2 = 0.509$, and Pe = 100 [panels (a) and (b)] and $\varepsilon_s/\varepsilon = 10$, $\rho\sigma^2 = 0.150$, and Pe = 500 [panels (d) and (e)]. Panels (a) and (d) show the swimming pressure, whereas panels (b) and (e) show the interacting pressure. Note that the color bars are not in the same scale. For a better visualization, panel (e) is a zoomed-in view of the system presented in panel (d) but with interacting pressure in the color code. Panels (c) and (f) show total pressure vs density for $\varepsilon_s/\varepsilon = 1$ and $\varepsilon_s/\varepsilon = 10$, respectively; different colors represent the value for Peclet number; continuous lines represent the density range where the system is in a homogeneous state and dashed lines represent the density range where MIPS occurs.

are anti-parallel. We postulate meanwhile the pure repulsive interaction force tries to avoid the aggregation, the active force tends to keep the particles in the dense phase. In the low density region, collision events are not often, and then, the value of the swimming pressure is higher than that in the high density region. Figures 6(b) and 6(e) represent the contribution from the interaction potential to the pressure for the two systems in an MIPS state. Even when we observe a high value of the pressure inside the dense phase, in panel (b) ($\varepsilon_s/\varepsilon = 1$), we appreciate higher values. When $\varepsilon/\varepsilon_s = 1$, particles in the dense phase are monomers interacting directly with the hard core as discussed above. On the other hand, when $\varepsilon_s/\varepsilon = 10$, in the dense phase, chains that are already overlapped can move through the shoulder without any important contribution to the force. Looking at Fig. 6(e) [zoomed-in view of Fig. 6(d) depicting the interacting pressure through the color code], particles with a high interactive pressure in the dense region are monomers interacting with the chains via soft shell. Finally, Figs. 6(c) and 6(f) show the global pressure for $\varepsilon_s/\varepsilon = 1$ and $\varepsilon_s/\varepsilon = 10$ as a function of the density in a range of Peclet number between 10 and 400. Here, the pressure is computed by means of Eq. (6) in both systems. At low density, the contribution from the interaction potential to the pressure is almost negligible. If we consider those conditions where the noise is small enough, the velocity of the particle is given by $\dot{\vec{r}}_i \approx \frac{D_t}{k_B T}|F_a|\,\vec{n}_i$ and the contribution of the activity to the pressure can be approximated to $P_s \approx \frac{1}{6}\,\mathrm{Pe}\,|F_a|\,\sigma\,\rho$. Hence, under these conditions, the total pressure is proportional to the number density, $P \approx \left(k_B T + \frac{1}{6}\,\mathrm{Pe}\,|F_a|\,\sigma\right)\rho$, as confirmed in Fig. 6. On the other hand, in the high density region, we observe two different behaviors. For $\varepsilon_s/\varepsilon = 1$, the pressure decreases drastically in the MIPS region (the dashed line), as was reported in Ref. 60. For $\varepsilon_s/\varepsilon = 10$, the system is almost frozen and the curves collapse. Figure 6(f) shows that the pressure is monotonic almost for all Pe values, but have an inflexion point around ρ_c. For densities above ρ_c and high enough activity, particles have access to the soft shell, so the contribution from the interaction potential to the pressure is smaller and then the total pressure decreases.

B. Dynamical features

As discussed earlier, suspensions characterized by $\varepsilon_s/\varepsilon = 1$ and $\varepsilon_s/\varepsilon = 100$ behave like those composed by ABPs interacting through a WCA potential, whose dynamical behavior was already studied in a previous study.[17] In this last section, we will mainly focus on the dynamics of systems where the shoulder height ($\varepsilon_s/\varepsilon = 10$) competes with the energy provided by activity.

1. Long time diffusion

In Fig. 7, we report the diffusion coefficient computed from the long time behavior of the mean square displacement as a function of the system density and activity. We distinguish three different behaviors: one detected at Pe = 0, one detected in the range between 0 < Pe <5, and another one for Pe >5. In the passive scenario,

D_{eff} monotonously decreases with density in the range between $0 < \rho\sigma^2 < 0.150$. Beyond this value, the system is in a closed packed state: particles move only when they cross the region delimited by the shoulder of their neighbors and the only relevant length scale is the width of shoulder.

When (0 < Pe <5), the long time diffusion coefficient increases with activity in the range $0 < \rho\sigma^2 < 0.15$, as expected. However, beyond the close-packing density, D_{eff} increases again because the combination of mild activity and high density allows some particles to overcome the shoulders of their neighbors and move more easily.

At a scaled density slightly below 0.2, the diffusion constant goes through a maximum, whereas it decays back to zero for higher densities. When the activity is high (Pe >5), the repulsive shoulder becomes almost irrelevant and D_{eff} decreases again monotonously over the whole density range, only dropping to zero at very high densities. The only sign of particles starting to overlap is the inflection point observed around $\rho\sigma^2 = 0.150$, which gets smoother as the activity increases, disappearing completely for Pe >140.

In order to unravel the differences in dynamical behavior between the passive and active cases, we focus on two particular densities $\rho\sigma^2 = 0.150$ (just above the close packing density) and $\rho\sigma^2 = 0.20$ (33% larger than the close packing density). When particles are passive and $\rho\sigma^2 = 0.15$, particles are mostly monomers forming a hexagonal lattice, whereas at $\rho\sigma^2 = 0.20$, the system is disordered and particles form mostly dimers and chains (not showed here). When Pe = 1 and $\rho\sigma^2 = 0.150$, monomers still form an hexagonal crystal and the single particle diffusion coefficient barely changes. However, at $\rho\sigma^2 = 0.20$, the inclusion of activity significantly changes the overall structures the chains disappear completely and dimers overall randomly distributed throughout the system. On the other hand, the diffusion coefficient increases by around two orders of magnitude with respect to the value measured in the passive system. At very high Peclet number (for example Pe ≈ 400), the behavior detected at both densities is very similar, with signs of MIPS, analogous local structure inside the dense phase, and comparable values of the diffusion coefficient. The only noticeable difference is the lower fraction of the dilute phase at higher density. To summarize, at $\rho = 0.150$, the system goes from stagnant at Pe < 2 to very fast diffusion at Pe > 2, with an increase of almost six orders of magnitude, while at $\rho\sigma^2 = 0.2$ monotonically changes from stagnant (at Pe = 0) to very fast diffusion at large Pe.

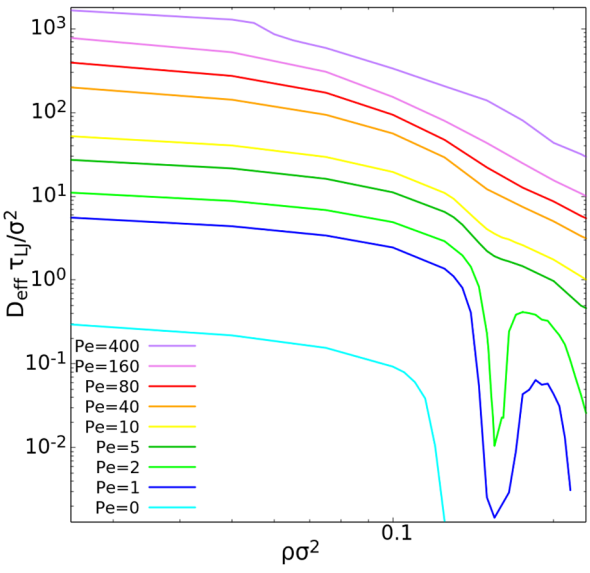

FIG. 7. Diffusion coefficient vs density for $\varepsilon_s/\varepsilon = 10$ and different values of the Peclet number, Pe = 0, 1, 2, 5, 10, 40, 80, 160, and 400.

A non-monotonic behavior of the diffusion coefficient has been already detected in suspensions of active glass formers (a binary mixture of WCA active Ornstein Uhlenbeck particles). In Ref. 65, the authors showed that the diffusion coefficient depended monotonically on the persistence time for a given volume fraction when the temperature was high. On the other hand, the diffusion coefficient was not monotonous with persistence time at low temperature. A similar non-monotonicity has been detected in Ref. 66 in an active Ornstein Uhlenbeck particles suspension.

2. Self-intermediate scattering function

A different qualitative dependence of the diffusion constant with respect to density observed in particles with low activity (Pe <5) and high activity (Pe >5) deserves a more detailed discussion. In this section, we explore the evolution of the mean-square displacement and the intermediate scattering function [Eq. (7)] for systems with $\varepsilon_s/\varepsilon = 10$, at different activities Pe = 1 and 10, and at densities that range from $\rho\sigma^2 = 0.145$ (slightly below the overlap density ρ_c) to $\rho\sigma^2 = 0.245$ (well beyond the overlap density). Both results are shown in Fig. 8. In Fig. 8(a), the MSD grows monotonically for both Pe = 1 (continuous lines) and Pe = 10 (dashed lines), but with qualitatively different behaviors. At Pe = 10, the MSD shows a short-lived superdiffusive regime (MSD $\propto t^{\alpha}$, with $\alpha > 1$) before moving to the terminal Fickian behavior, while the MSD decreases monotonically with density, as expected from the results shown in Fig. 7. Since the activity is large enough to overcome the effect of the soft shell, the dynamics is only determined by the hard core potential, and the system reproduces the behavior depicted by solutions of ABPs interacting through a potential with a single relevant length scale in the range between small and medium densities. At low activity (Pe = 1, continuous lines), the MSD shows a completely different qualitative behavior. First, it goes through a long-lived subdiffusive behavior regime ($\alpha < 1$) before reaching the terminal Fickian regime. On the other hand, the dependence of the MSD with density is not monotonous. This rich diffusive behavior is also reflected in the self-intermediate scattering function, which is represented in Fig. 8(b). For large activities (Pe = 10), $F(q^*, t)$ decays almost as a single exponential, which is the characteristic behavior of a particle diffusing in the Fickian regime. However, for small activity (Pe = 1), it decrease much slower, with signs of the two-stage relaxation characteristic of glassy behavior. In particular, at small densities ($\rho\sigma^2 < 0.187$), a two-step decay is clearly observed. The emergence of the fast decay suggests that, at these densities, most particles diffuse along short distances or, equivalently, they are trapped inside a cage. Only at long times, when the collective motion of particles opens the cage, particles can escape and $F(q^*, t)$ decays to zero. The terminal decay time, related to the long time diffusion coefficient, is again not monotonic, as expected from the results depicted

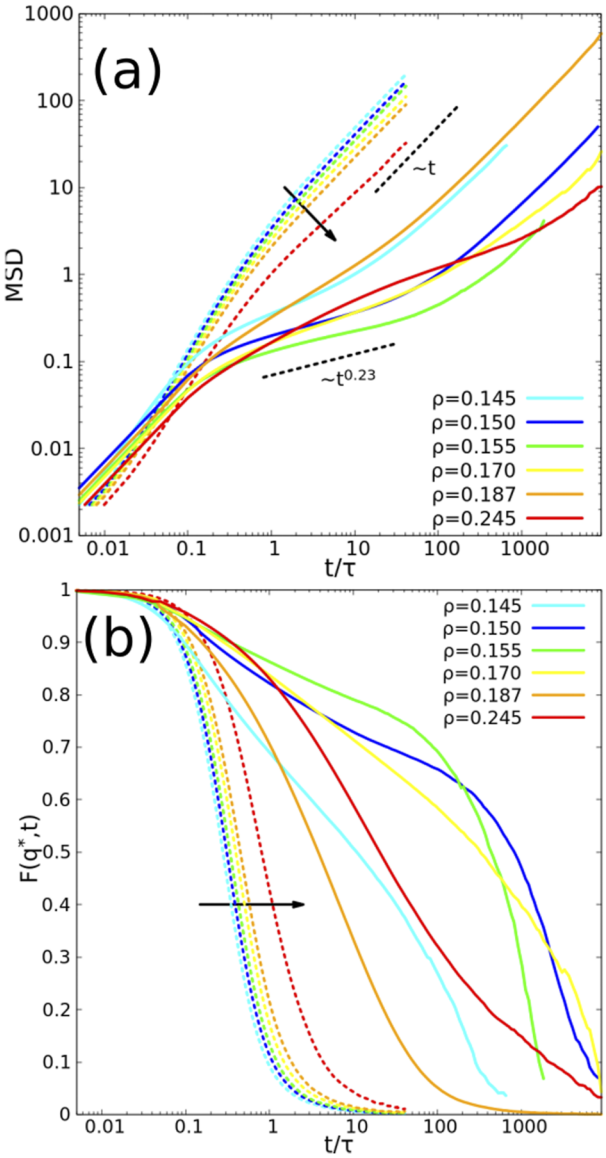

FIG. 8. (a) Mean Square Displacement (MSD) for the system and (b) $F(q^*,t)$ vs simulation time for $\varepsilon/\varepsilon_s = 10$ and two different values of the Peclet number, Pe = 1 (continuous line) and Pe = 10 (dashed line). The densities used are showed in the legend.

in Fig. 7. At higher densities ($\rho\sigma^2 = 0.187$), the overlap of particles allows them to access the space of the soft shell and move more freely, which is reflected in the decay of $F(q^*,t)$, which now looks more like an stretched exponential, a characteristic of a collection of diffusive particles that present a wide distribution of diffusion coefficients. Finally, when the density increases again ($\rho\sigma^2 = 0.245$), the system slows down again due to the increased density, as explained above, when discussing the mean-squared displacement.

As shown in Ref. 67, an active glass former (ABP interacting via Kob Anderson) shows a thermal aging when the persistence time is small. On the other hand, when the persistence time is large, aging happens via two steps: active athermal aging at short times and activity-driven aging at long times.

IV. CONCLUSIONS

In this work, we study a system of Active Brownian Particles (ABPs) interacting through a continuous shoulder potential. Even for the passive case, many interesting phenomena arise and particles self-organize in complex local structures (monomers, dimers, trimers, chains, and others). One of the main points of this work is to characterize these structures and to study how the fraction of each one changes with the activity, focusing on the range of densities and activities where the system presents MIPS.

At a constant propulsion velocity, we study three different values for the shoulder barrier strength, $\varepsilon_s/\varepsilon = 1$, 10, and 100. Depending on the relative size of the activity and the strength of the soft shell barrier, the particles can overlap the shoulders of their neighbors easily or not. In the cases $\varepsilon_s/\varepsilon = 1$ and 100, just one length scale is relevant and, given that the shoulder potential is approximately equivalent to a WCA potential with an effective diameter, we can map the phase diagram for this two barrier values with the WCA one. We focus on the case $\varepsilon_s/\varepsilon = 10$ when the soft shell and the hard core are both relevant for the dynamics of the system. In this case, the system also presents, for some values of density and Peclet number, a Motility Induce Phase Separation (MIPS) region characteristic of active systems but, in contrast with the results found for the single length scale case, the structures found inside the MIPS state are not hexagonal. To better understand the case when the activity and the strength of the soft shell are similar, we explore the equation of state and find that it is clearly different from the single length scale scenario. If the potential only has one relevant length scale, the pressure shows a discontinuity when the system enters the MIPS state due to the separation in low and high density regions. On the other hand, when the two length scales play a relevant role in the system, this transition is much smoother.

Finally, we have explored the dynamical features of the system when both length scales are relevant by studying the MSD and the self-intermediate scattering function. Our results show that, in the low activity regime, the topological cage produced by the soft shell promotes non-monotonic increase of the diffusion coefficient with density. When this cage is efficient, the particles barely move through the system. However, if the activity is strong enough, particles can overlap each other and have access to more space to diffuse easily.

Recently, Refs. 68 and 69 have experimentally shown that the approach to glass transition in an active system can be mapped onto a passive supercooled liquid of soft colloids. However, the mapping failed beyond the glass transition, where a non-monotonic response of the relaxation time appeared. The authors suggested that the non-monotonicity could be caused by two competing effects due to activity: an extra energy causing cage breaking and propulsion's directionality hindering cage exploration. Therefore, they concluded that the many-body nature of cooperative motion should be taken into account when dealing with active glasses.

On the one hand, our work demonstrates that active colloids characterized by two repulsive length scales show an anomalous dynamics qualitatively similar to that observed in passive glasses

characterized by two repulsive length scales. On the other hand, since our results resemble those presented in Refs. 68 and 69, we might state that the conclusions drawn in Refs. 68 and 69 hold for active particles characterized by either one or two repulsive length scales. Therefore, the anomalous dynamics in a dense suspension of active Brownian particles interacting via the shoulder potential is due to a synergy effect of the two repulsive length scales in combination with the activity.

SUPPLEMENTARY MATERIAL

In the supplementary material, we report (1) the non-Gaussian parameter for few case studies, (2) structures characterizing the passive system with $\varepsilon_s = 10$, and (3) plots of the velocity fields for the system with $\varepsilon_s = 10$.

ACKNOWLEDGMENTS

C. Valeriani and F. Martínez-Pedrero acknowledge funding from Ministerio de Asuntos Económicos y Transformación Digital (MINECO) (Grant No. PID2019-105343GB-I00). C. Valeriani acknowledges funding from MINECO (Grant No. EUR2021-122001). J. Ramírez acknowledges funding from MINECO (Grant No. PID2019-105898GA-C22).

AUTHOR DECLARATIONS

Conflict of Interest

The authors have no conflicts to disclose.

DATA AVAILABILITY

The data that support the findings of this study are available from the corresponding author upon reasonable request.

REFERENCES

[1] S. Ramaswamy, J. Stat. Mech.: Theory Exp. **2017**, 054002.
[2] C. Bechinger, R. D. Leonardo, H. Lowen, C. Reichhardt, G. Volpe, and G. Volpe, Rev. Mod. Phys. **88**, 045006 (2016).
[3] T. Vicsek and A. Zafeiris, Phys. Rep. **517**, 71 (2012).
[4] J. Yan, M. Han, J. Zhang, C. Xu, E. Luijten, and S. Granick, Nat. Mater. **15**, 1095 (2016).
[5] A. Snezhko and I. S. Aranson, Nat. Mater. **10**, 698 (2011).
[6] Y. Fily and M. C. Marchetti, Phys. Rev. Lett. **108**, 235702 (2012).
[7] G. S. Redner, M. F. Hagan, and A. Baskaran, Phys. Rev. Lett. **110**, 055701 (2013).
[8] J. Stenhammar, D. Marenduzzo, R. J. Allen, and M. E. Cates, Soft Matter **10**, 1489 (2014).
[9] J. Bialké, H. Löwen, and T. Speck, Europhys. Lett. **103**, 30008 (2013).
[10] J. T. Siebert, F. Dittrich, F. Schmid, K. Binder, T. Speck, and P. Virnau, Phys. Rev. E **98**, 030601 (2018).
[11] A. Wysocki, R. G. Winkler, and G. Gompper, Europhys. Lett. **105**, 48004 (2014).
[12] A. K. Omar, K. Klymko, T. GrandPre, and P. L. Geissler, "Phase diagram of active Brownian spheres: Crystallization and the metastability of motility-induced phase separation," Phys. Rev. Lett. **126**, 188002 (2021).
[13] N. de Macedo Biniossek, H. Löwen, T. Voigtmann, and F. Smallenburg, J. Phys.: Condens. Matter **30**, 074001 (2018).
[14] P. Digregorio, D. Levis, A. Suma, L. F. Cugliandolo, G. Gonnella, and I. Pagonabarraga, Phys. Rev. Lett. **121**, 098003 (2018).
[15] D. Levis, J. Codina, and I. Pagonabarraga, Soft Matter **13**, 8113 (2017).
[16] P. Digregorio, D. Levis, A. Suma, L. F. Cugliandolo, G. Gonnella, and I. Pagonabarraga, J. Phys.: Conf. Ser. **1163**, 012073 (2019).
[17] J. Martin-Roca, R. Martinez, L. C. Alexander, A. Luis Diez, D. G. A. L. Aarts, F. Alarcon, J. Ramírez, and C. Valeriani, J. Chem. Phys. **154**, 164901 (2021).
[18] M. Paoluzzi, D. Levis, and I. Pagonabarraga, "How does motility-induced phase-separation interplay with glassiness in dense active matter?," arXiv:2109.14948 (2021).
[19] L. Berthier and J. Kurchan, "Non-equilibrium glass transitions in driven and active matter," Nat. Phys. **9**, 310–314 (2013).
[20] R. Ni, M. A. Cohen Stuart, and M. Dijkstra, "Pushing the glass transition towards random close packing using self-propelled hard spheres," Nat. Commun. **4**, 2704 (2013).
[21] K. Paul, S. K. Nandi, and S. Karmakar, "Dynamic heterogeneity in active glass-forming liquids is qualitatively different compared to its equilibrium behaviour," arXiv:2105.12702 (2021).
[22] S. K. Nandi, R. Mandal, P. J. Bhuyan, C. Dasgupta, M. Rao, and N. S. Gov, "A random first-order transition theory for an active glass," Proc. Natl. Acad. Sci. U. S. A. **115**, 7688–7693 (2018).
[23] R. Mandal, P. J. Bhuyan, P. Chaudhuri, C. Dasgupta, and M. Rao, "Extreme active matter at high densities," Nat. Commun. **11**, 2581 (2020).
[24] J. Smrek, I. Chubak, C. N. Likos, and K. Kremer, "Active topological glass," Nat. Commun. **11**, 26 (2020).
[25] P. C. Hemmer and G. Stell, Phys. Rev. Lett. **24**, 1284 (1970).
[26] G. Malescio, J. Phys.: Condens. Matter **19**, 073101 (2007).
[27] M. R. Sadr-Lahijany, A. Scala, S. V. Buldyrev, and H. E. Stanley, Phys. Rev. E **60**, 6714 (1999).
[28] P. Kumar, S. V. Buldyrev, F. Sciortino, E. Zaccarelli, and H. E. Stanley, Phys. Rev. E **72**, 021501 (2005).
[29] E. A. Jagla, J. Chem. Phys. **111**, 8980 (1999).
[30] F. H. Stillinger and D. K. Stillinger, Physica A **244**, 358 (1997).
[31] A. Barros de Oliveira, P. A. Netz, T. Colla, and M. C. Barbosa, J. Chem. Phys. **124**, 084505 (2006).
[32] J. Mittal, J. R. Errington, and T. M. Truskett, J. Chem. Phys. **125**, 076102 (2006).
[33] H. M. Gibson and N. B. Wilding, Phys. Rev. E **73**, 061507 (2006).
[34] P. J. Camp, Phys. Rev. E **71**, 031507 (2005).
[35] A. B. de Oliveira, G. Franzese, P. A. Netz, and M. C. Barbosa, J. Chem. Phys. **128**, 064901 (2008).
[36] L. Xu, S. V. Buldyrev, C. A. Angell, and H. E. Stanley, Phys. Rev. E **74**, 031108 (2006).
[37] M. Asai, A. Cacciuto, and S. K. Kumar, "Surface fluctuations dominate the slow glassy dynamics of polymer-grafted colloid assemblies," ACS Cent. Sci. **4**, 1179–1184 (2018).
[38] G. Franzese, "Differences between discontinuous and continuous soft-core attractive potentials: The appearance of density anomaly," J. Mol. Liq. **136**, 267–273 (2007).
[39] A. J. Schultz, C. K. Hall, and J. Genzer, "Computer simulation of block copolymer/nanoparticle composites," Macromolecules **38**, 3007–3016 (2005).
[40] G. Malescio and G. Pellicane, "Stripe patterns in two-dimensional systems with core-corona molecular architecture," Phys. Rev. E **70**, 021202 (2004).
[41] N. V. Gribova, Y. D. Fomin, D. Frenkel, and V. N. Ryzhov, "Waterlike thermodynamic anomalies in a repulsive-shoulder potential system," Phys. Rev. E **79**, 051202 (2009).
[42] L. Caprini, E. Hernández-García, and C. López, "Cluster crystals with combined soft- and hard-core repulsive interactions," Phys. Rev. E **98**, 052607 (2018).
[43] Z. Yan, S. V. Buldyrev, P. Kumar, N. Giovambattista, and H. E. Stanley, "Correspondence between phase diagrams of the TIP5P water model and a spherically symmetric repulsive ramp potential with two characteristic length scales," Phys. Rev. E **77**, 042201 (2008).
[44] N. M. Barraz, Jr., E. Salcedo, and M. C. Barbosa, "Thermodynamic, dynamic, and structural anomalies for shoulderlike potentials," J. Chem. Phys. **131**, 094504 (2009).

[45]J. Horbach, "Molecular dynamics computer simulation of amorphous silica under high pressure," J. Phys.: Condens. Matter **20**, 244118 (2008).
[46]G. Foffi, F. Sciortino, P. Tartaglia, E. Zaccarelli, F. L. Verso, L. Reatto, K. A. Dawson, and C. N. Likos, "Structural arrest in dense star-polymer solutions," Phys. Rev. Lett. **90**, 238301 (2003).
[47]M. Sperl, E. Zaccarelli, F. Sciortino, P. Kumar, and H. E. Stanley, "Disconnected glass-glass transitions and diffusion anomalies in a model with two repulsive length scales," Phys. Rev. Lett. **104**, 145701 (2010).
[48]N. Gnan, G. Das, M. Sperl, F. Sciortino, and E. Zaccarelli, "Multiple glass singularities and isodynamics in a core-softened model for glass-forming systems," Phys. Rev. Lett. **113**, 258302 (2014).
[49]K. N. Pham, A. M. Puertas, J. Bergenholtz, S. U. Egelhaaf, A. Moussaïd, P. N. Pusey, A. B. Schofield, M. E. Cates, M. Fuchs, and W. C. K. Poon, "Multiple glassy states in a simple model system," Science **296**, 104–106 (2002).
[50]H. Brenner, "Coupling between the translational and rotational Brownian motions of rigid particles of arbitrary shape I. Helicoidally isotropic particles," J. Colloid Sci. **20**, 104–122 (1965).
[51]S. Plimpton, "Fast parallel algorithms for short-range molecular dynamics," J. Comput. Phys. **117**, 1–19 (1995).
[52]R. P. Peláez (2021). "Universally adaptable multiscale molecular dynamics (UAMMD)," Github. https://github.com/RaulPPelaez/UAMMD.
[53]J. D. Weeks, D. Chandler, and H. C. Andersen, "Role of repulsive forces in determining the equilibrium structure of simple liquids," J. Chem. Phys. **54**, 5237–5247 (1971).
[54]F. Ginelli and H. Chaté, "Relevance of metric-free interactions in flocking phenomena," Phys. Rev. Lett. **105**, 168103 (2010).
[55]S. A. Mallory, A. Šarić, C. Valeriani, and A. Cacciuto, "Anomalous thermomechanical properties of a self-propelled colloidal fluid," Phys. Rev. E **89**, 052303 (2014).
[56]S. C. Takatori, W. Yan, and J. F. Brady, "Swim pressure: Stress generation in active matter," Phys. Rev. Lett. **113**, 028103 (2014).
[57]A. P. Solon, Y. Fily, A. Baskaran, M. E. Cates, Y. Kafri, M. Kardar, and J. Tailleur, "Pressure is not a state function for generic active fluids," Nat. Phys. **11**, 673–678 (2015).
[58]T. Speck and R. L. Jack, "Ideal bulk pressure of active Brownian particles," Phys. Rev. E **93**, 062605 (2016).
[59]F. Ginot, I. Theurkauff, D. Levis, C. Ybert, L. Bocquet, L. Berthier, and C. Cottin-Bizonne, "Nonequilibrium equation of state in suspensions of active colloids," Phys. Rev. X **5**, 011004 (2015).
[60]M. Sanoria, R. Chelakkot, and A. Nandi, "Influence of interaction softness on phase separation of active particles," Phys. Rev. E **103**, 052605 (2021).
[61]R. G. Winkler, A. Wysocki, and G. Gompper, "Virial pressure in systems of spherical active Brownian particles," Soft Matter **11**, 6680–6691 (2015).
[62]L. Caprini, U. M. B. Marconi, C. Maggi, M. Paoluzzi, and A. Puglisi, "Hidden velocity ordering in dense suspensions of self-propelled disks," Phys. Rev. Res. **2**, 023321 (2020).
[63]L. Caprini and U. Marini Bettolo Marconi, "Spatial velocity correlations in inertial systems of active Brownian particles," Soft Matter **17**, 4109–4121 (2021).
[64]L. Caprini, U. Marini Bettolo Marconi, and A. Puglisi, "Spontaneous velocity alignment in motility-induced phase separation," Phys. Rev. Lett. **124**, 078001 (2020).
[65]L. Berthier, E. Flenner, and G. Szamel, "How active forces influence nonequilibrium glass transitions," New J. Phys. **19**, 125006 (2017).
[66]L. Caprini, F. Cecconi, A. Puglisi, and A. Sarracino, "Diffusion properties of self-propelled particles in cellular flows," Soft Matter **16**, 5431–5438 (2020).
[67]R. Mandal and P. Sollich, "Multiple types of aging in active glasses," Phys. Rev. Lett. **125**, 218001 (2020).
[68]N. Klongvessa, F. Ginot, C. Ybert, C. Cottin-Bizonne, and M. Leocmach, "Active glass: Ergodicity breaking dramatically affects response to self-propulsion," Phys. Rev. Lett. **123**, 248004 (2019).
[69]N. Klongvessa, F. Ginot, C. Ybert, C. Cottin-Bizonne, and M. Leocmach, "Nonmonotonic behavior in dense assemblies of active colloids," Phys. Rev. E **100**, 062603 (2019).